Physical modeling of the creep response of an Al–Cu–Mg alloy with a fine microstructure transformed by Friction Stir Processing

Physical modeling of the creep response of an Al-Cu-Mg alloy with a fine microstructure transformed by Friction Stir Processing

E. Santecchia[1,2,*], M. Cabibbo[3], M. Ghat[3], M. Regev[4], S. Spigarelli[3]

1. Consorzio Interuniversitario Nazionale per la Scienza e Tecnologia dei Materiali (INSTM - UdR Ancona), Italy

2. SIMAU, Università Politecnica delle Marche, via Brecce Bianche 60131 Ancona, Italy

3. DIISM, Università Politecnica delle Marche, via Brecce Bianche 60131 Ancona, Italy

4. Mechanical Engineering Department, ORT Braude College, P.O. Box 78, Karmiel 2161002, Israel

https://doi.org/10.1016/j.msea.2019.138521

Received 1 August 2019; Received in revised form 4 October 2019; Accepted 5 October 2019

available online 9 October 2019

Physical modeling of the creep response of an Al-Cu-Mg alloy with a fine microstructure transformed by Friction Stir Processing

E. Santecchia[1,2,*], M. Cabibbo[3], M. Ghat[3], M. Regev[4], S. Spigarelli[3]

1. Consorzio Interuniversitario Nazionale per la Scienza e Tecnologia dei Materiali (INSTM - UdR Ancona), Italy

2. SIMAU, Università Politecnica delle Marche, via Brecce Bianche 60131 Ancona, Italy

3. DIISM, Università Politecnica delle Marche, via Brecce Bianche 60131 Ancona, Italy

4. Mechanical Engineering Department, ORT Braude College, P.O. Box 78, Karmiel 2161002, Israel

Abstract

The creep response of an Al-Cu-Mg 2024 Aluminum alloy with a refined microstructure produced by Friction Stir Processing (FSP) has been investigated. The material, after FSP, exhibited a strong reduction in creep resistance, attested by higher values of the minimum creep rate, when compared with the base metal (the AA2024 in T3 state). A constitutive model based on a theoretical approach has been then used to correlate microstructural features and creep properties. The model was modified to take into account the microstructure of the transformed alloy, with a fine recrystallized grain size and lower mechanical strength. The hardness variation with creep duration was used to quantify the particle strengthening term. The resulting model gave an excellent description of the experimental results, without requiring any data-fitting of the minimum creep rate experimental data. This achievement represents a substantial advantage over conventional approaches based on phenomenological equations.

Introduction

The creep response of metals and alloys has been traditionally studied by establishing correlations between the mechanical data (usually in form of minimum creep rate, stress and temperature) and the microstructural features. In this context, several constitutive models, usually based on power-laws and Arrhenius equation, have been established and successfully used to interpolate the experimental data. Once the data-fitting is complete, the different parameters that appear in these equations are variously correlated with the available evidences on microstructure. An example of this procedure can be found in [1-3], which dealt with an annealed AA2024 aluminium alloy produced by powder-metallurgy. This approach is still in use, and maintains a good effectiveness, primarily because it can be simply handled. Yet, this traditional procedure has an obvious weakness, that is, it is based on constitutive equations of phenomenological nature, which require the fitting of experimental data to be properly used. Basic modelling tries to overcome this weakness by proposing constitutive equations entirely based on theoretical works, which, in principle, should not need minimum creep-data fitting. These models, on the other hand, require the detailed knowledge of several microstructural data, such as, for example, the dislocation density, the grain size, the amount of elements in solid solution, the volume fraction, particle size and interparticle spacing of the strengthening precipitates etc., and of their evolution during creep.

One of the most interesting basic models has been developed to describe the creep response of pure Cu, by Sandström and co-workers [4-6]. The model has been later implemented to describe pure Al [7], Al-Mg solid solution alloys [8], Al-based composites [9] and, last but not least, an age-hardening Al alloy (the AA2024-T3) [10]. In the last case, the microstructural instability typical of age-hardening alloys when exposed at high temperature required a complex modelling of the softening phenomena, mainly driven by the stress-accelerated coarsening of the precipitates. In addition, the peculiar nature of the hardening phases, dispersed in form of coarse intergranular precipitates and intermetallic phases and of fine intragranular elongated rods, had to be accounted for. In addition, also the effect of grain size had to be quantified, since the original models were developed for coarse-

grained materials. Although the model provided an excellent description of the experimental data, the use of a number of complex equations and the need for extensive microstructural information may constitute a substantial hindrance to its wider application. The present study is an attempt to address this critical issue. The first goal here pursued is the application of the constitutive model proposed for AA2024-T3 alloy in [10], to the same material, but with a different initial microstructure. In principle, the model should be able to successfully describe the creep response irrespective of the initial state, if sufficient information of the initial microstructure and of its evolution during creep is available. This point directly leads to the second goal of the study, that is, to provide a simpler method for describing the softening phenomena associated to the hardening phase evolution, rather than the complex equations used in [10].

The T3 state consists in solution-treatment, cold working and natural ageing up to a stable condition. This combination of heat treatment and cold working produces an extremely complex microstructure [11]. In one case, for example, the 60% of the particles between 500 and 700 nm in size were identified as equilibrium S-phase (Al_2CuMg) precipitates; another study [12] found a multitude of phases of different chemistry, including S and θ (Al_2Cu) phases and others containing Cu, Fe, Mn, Si and Mg. The two mentioned studies specifically considered the corrosion properties of the alloy and were thus mainly focused on coarse precipitates and intermetallics, which have little or no influence on dislocation slip. By contrast, creep response is dramatically influenced by the presence of nano-sized precipitates, such as the S-phase rods that form after exposure at high temperature.

The complex microstructure of the AA2024 in the T3 state had to be transformed to properly address the first goal of the present study. This transformation was produced by applying Friction Stir Processing (FSP) to the AA2024-T3 plates [13]. Friction Stir Processing is a severe plastic deformation process directly derived from Friction Stir Welding (FSW), a process developed at The Welding Institute (TWI) in the UK in 1991 [14,15]. The aim of FSP is to obtain a stir zone with very fine grain size. For this purpose, as in FSW, a non-consumable rotating tool with a shoulder and a pin traverses the parent material and produces intense plastic deformation.

During FSP, the elongated grains of the parent AA2024-T3 changed into fine equiaxed ones by a Dynamic Recrystallization process. The two kinds of particles in the alloy in T3 state, namely, the very coarse precipitates and intermetallic phases, tens of microns in size and the evenly dispersed nano-sized precipitates, also underwent substantial changes after FSP. The coarse precipitates and intermetallic phases, in particular, were broken into more uniformly dispersed 0.1-1 μm particles. Due to the grain refining process (the grain size decreased down to 5 μm, i.e. of one order of magnitude), most of these particles were again located on grain boundaries. As a result of the dramatic alterations of the structure due to deformation and heating (grain refining by DRX and changes in nature, volume fraction, size and distribution of the strengthening intragranular precipitates), the tensile properties of the FSP processed material were inferior to those of the parent material. The average yield stress of the FSP material was about 22% lower than the average yield stress of the parent material in T3 state, while the tensile stress and the elongation to fracture dropped by about 25% and 71%, respectively. Hardness was found to greatly vary along the thickness and in transversal direction of the FSP zone, in many cases being substantially lower than the value for parent material [13]. These evidences seem to support the idea that, although fine intragranular precipitates still exists in the FSP alloy, they are less effective than in the T3 state to obstruct dislocation mobility, presumably because they are more widely spaced. Since FSP resulted in a marked heating of the alloy, followed by rapid cooling, partial dissolution or moderate coarsening of the precipitates is indeed likely to occur. In addition, as in the case of the T3 state, the transformed microstructure of the processed materials is thermally unstable. After 280 hours of exposure to 300°C, more extensive grain boundary decoration by large precipitates was indeed observed, together with the appearance of fine platelet-like precipitates, which are essentially rod-shaped, inside the grains [13].

On the basis of the information summarised above, one can safely conclude that the microstructure of the AA2024 alloy after FSP is sufficiently different to that of the parent AA2024-T3 to be an optimum candidate to test the validity of the model discussed in [10]. On the other hand, the FSP

alloy presents such a complex microstructure to make the use of the equations proposed in [10] scarcely viable, thus requiring a different approach to evaluate the softening phenomena.

Experimental procedures

The material considered in this study was a commercial AA2024-T3 aluminum alloy in the form of 200 mm x100 mm plates, 3 mm thick. The plates underwent FSP using a SHARNOA CNC milling machine. The H-13 steel welding/processing tool used consisted of a pin of 4.5 mm diameter and 3 mm height and a 20 mm diameter shoulder. A single pass was made on one side of the plate. The plate was then reversed and processed once again right above the first pass, which was now on the bottom side of the plate. The second pass was made so that the advancing side of the first pass became the retreating side of the second, and vice versa. The motivation was to make the stir zone as symmetrical and uniform as possible while achieving an almost rectangular cross-section. The optimal welding parameters were found to be a rotational speed of 800 rpm and a transverse speed of 80 mm/min. The processing parameters were selected by trial and error and subsequently by using visual examination, optical metallography of the cross-section and radiography [13].

Creep sample with the geometry reported in [13] (3 mm x 3 mm transversal section and 25 mm gauge length) were machined from the FSP region of the plates. The longitudinal axis of the samples was parallel to the FSP direction, so that the whole body of the specimen was included in the stir-zone. A three-zone furnace was used for heating the sample up to testing temperature; temperature was measured by four thermocouples (three for furnace control and one for data recording), two placed in correspondence of the center of the gauge length and the other two just above and below the specimen grips. Temperature variation was maintained within ±1°C along the gauge length, and maximum allowed deviation from the fixed temperature was ± 3°C. Elongation was continuously measured by Linear Variable Differential Transformer (LVDT).

Constant load creep experiments (CLE) were carried out on the samples at 250 and 315°C, in most cases up to sample fracture. Additional variable load experiments (VLE) were carried out at the same

temperature. In these experiments, the initial stress (50 MPa at 250°C, and 12 MPa at 315°C) was maintained until the onset of the minimum creep rate range. Then, the applied stress was abruptly increased one of two times, and maintained up to sample rupture.

TEM discs were mechanically thinned and polished before using a Struers™ Tenupol-5® electropolisher by which discs were prepared to electron transparency using a solution of 1/3 HNO_3 in methyl alcohol at V =12V and T = -35°C. Three discs per experimental condition were inspected. Inspections were carried out by using a Philips™ CM-200® transmission electron microscope, operated at 200 keV and equipped with double tilt specimen holder. Quantitative analysis of precipitates was carried out on crystallographic Al-[200] planes, according to conventional stereology methods [16], using Image Pro-Plus® software. The quantitative evaluation of volume, F_V, number fraction, N_V, spacing, λ, and mean size, d_{spp}, of the detected rod precipitates was thus carried out on statistically meaningful number of elements (*i.e.*, at least 300 per experimental condition). These data were measured by commonly used stereology relationships as the ones reported in some previously published papers by one of the present authors ([17], to cite but one).

Experimental results

Initial microstructure

Figure 1 shows representative images of the microstructure of the alloy after FSP. As attested in [13], FSP resulted in the formation of relatively large precipitates on the new grain boundaries. In addition, very fine precipitates can be observed in the fine-grain interiors. The extremely fine grain size (5μm), in principle, should provide a substantial increase of the strength due to the grain boundaries acting as barriers to dislocation motion. By contrast, both the ultimate tensile strength and the yield stress of the FSP alloy are substantially lower than those of the parent 2024-T3 (355 and 284 *vs* 464 and 362 for yielding and rupture for FSP and base alloys respectively [13]).

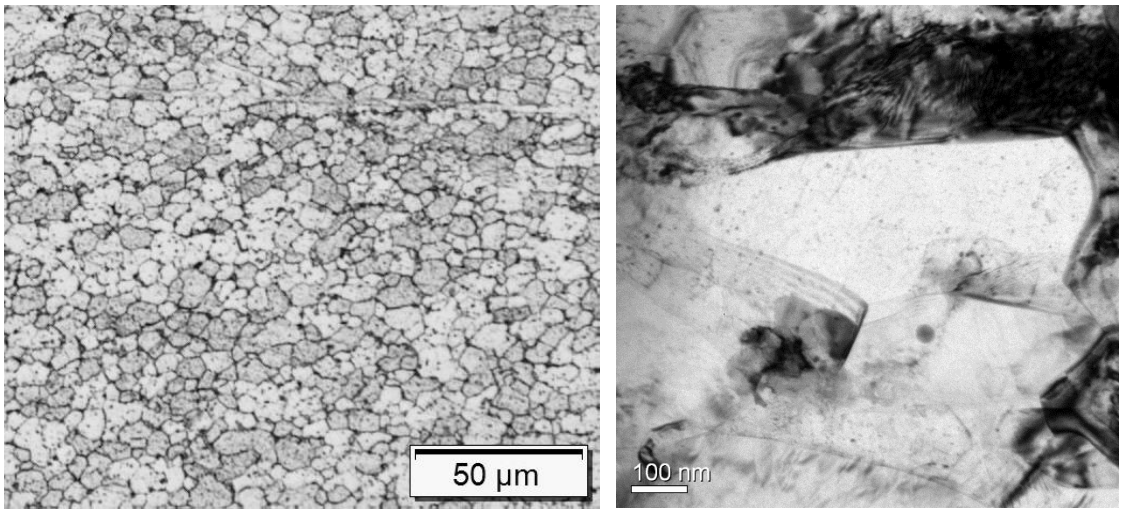

Figure 1. Microstructure of the FSP 2024-T3 alloy: a) optical micrograph; b) structure observed by TEM.

Figure 2 shows the variation of microhardness along the thickness of the FSP zone, in the central region of the transformed zone. Hardness is maximum on one of the plate surfaces (≅128 HV), then progressively decreases down to a minimum (≅113 HV, just in the mid-section), and then again increases, although the value on the second plate face remains a bit lower than the one measured on the opposite surface. The average hardness value (≅118 HV) is so close to the hardness measured on the softer surface, to consider this latter as representative of the whole sample. All these values are much lower than the hardness of the parent alloy (≅144 HV).

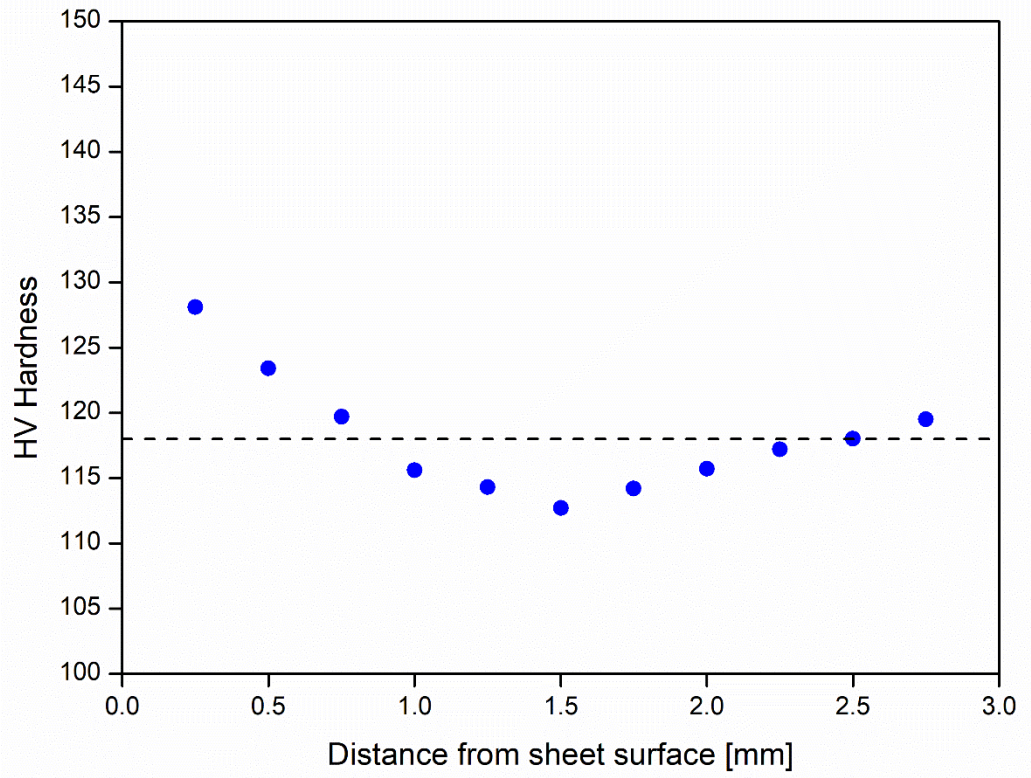

Figure 2. Vickers hardness variation along the thickness of the FSP 2024-T3 alloy, measured in the center of the FSP zone. The broken line represents the average HV value.

Creep data

Figure 3 shows the minimum creep rate data for the FSP 2024-T3 alloy, compared with the model curve calculated in similar testing condition for the parent alloy [10]. The Figure clearly shows that FSP results in substantially higher creep rate. A significant scatter of the experimental data was indeed observed in the high-stress regime at 250°C (120-140 MPa).

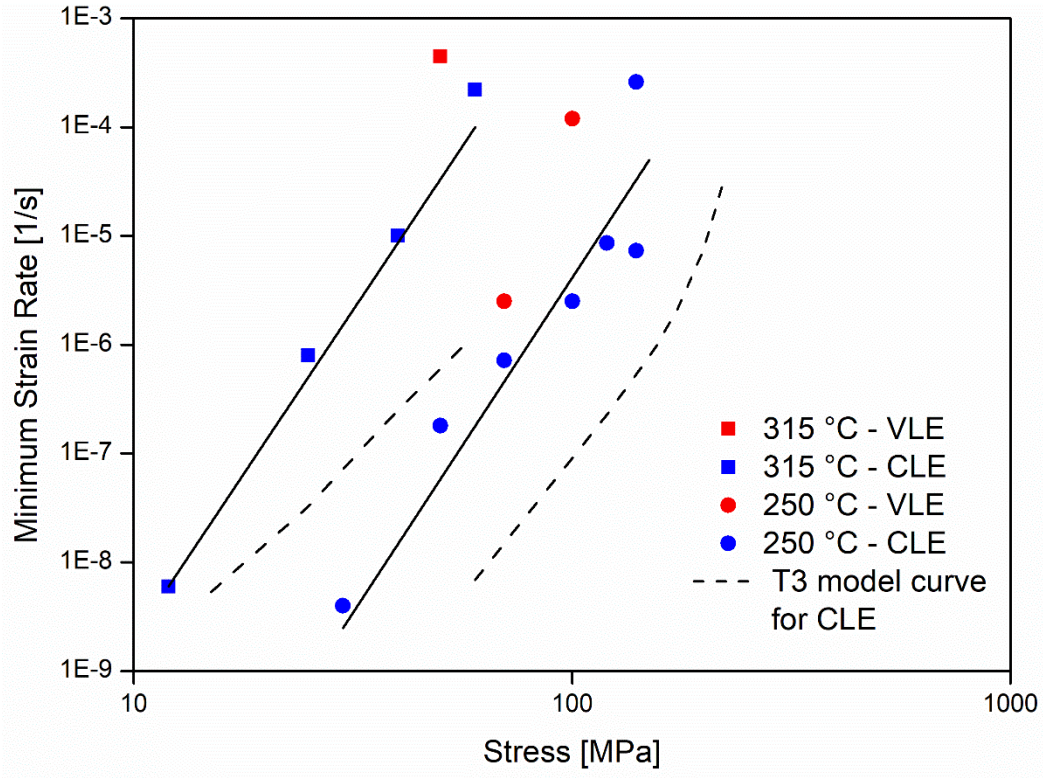

Figure 3. Minimum creep rate dependence on applied stress for 2024-T3 FSP alloy, tested both in constant (CLE) and variable (VLE) load conditions. The Figure also shows the strain rate for the base alloy tested by CLE (broken curves).

Figure 3 also plots the model curves obtained for 2024-T3 alloy at 250 and 315°C, calculated following the procedure described in [10].

The temperature dependence of the minimum strain rate was calculated by the usual procedure, based on the phenomenological equation (Eq. (1)):

$$\dot{\varepsilon}_m = A(\sigma)\exp\left(-\frac{Q}{RT}\right) \qquad (1)$$

where Q is the apparent activation energy for creep, and $A(\sigma)$ is a stress-dependent parameter. Calculation gives Q=260 kJ mol^{-1}, which is much higher than the activation energy for self-diffusion (122 kJ mol^{-1} [7]). This high value of the activation energy again clearly indicates that in this complex alloy, the microstructure is thermally unstable, i.e. it undergoes significant changes during prolonged holding at high temperature, as occurred in the case of the parent material [10]. This fact is confirmed

by the substantially higher values of the minimum strain rate obtained in VLE when compared with CLE carried out under the same stress. A similar behaviour can be explained by the progressive softening of the microstructure as the time of exposure at high temperature under a given applied load increases.

Figure 4 shows the Zener-Hollomon parameter Z (Eq. (2)):

$$Z = \dot{\varepsilon}_m \exp\left(\frac{Q}{RT}\right) \qquad (2)$$

as a function of the applied stress. As expected, with Q=260 kJ mol^{-1}, all the experimental data overlap on the same curve.

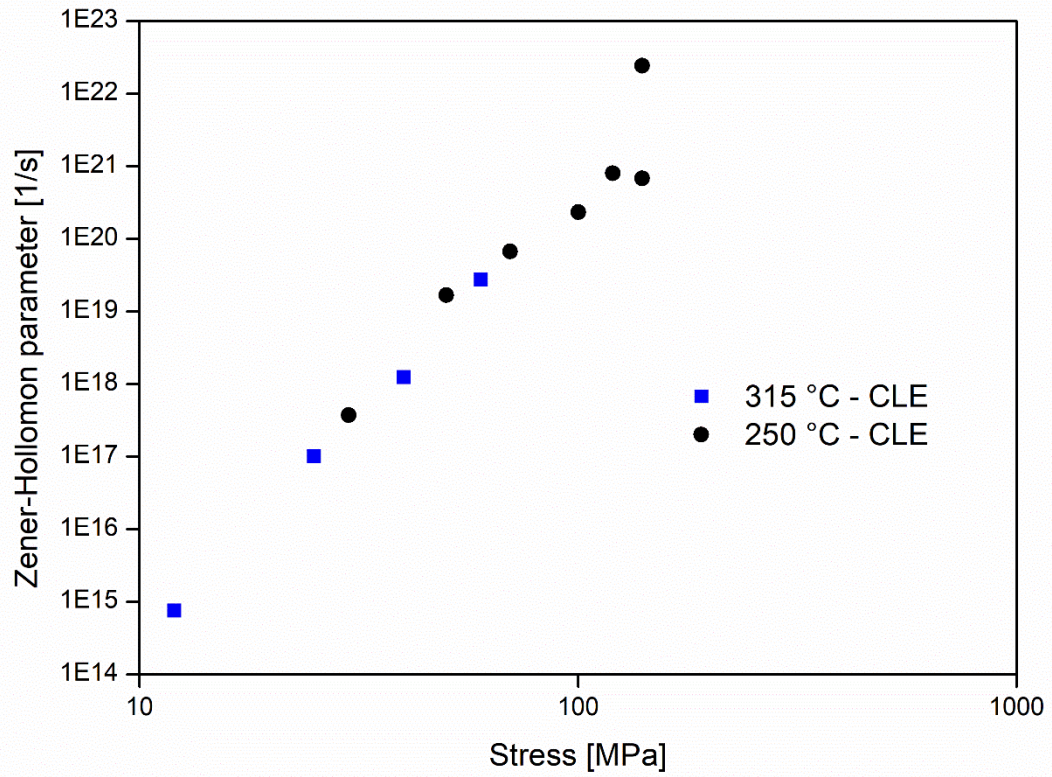

Figure 4. Zener-Hollomon parameter as a function of applied stress for 2024-T3 FSP tested under constant load conditions.

Microstructural evolution during creep

The initial microstructure, already softer for FSP alloy than in the parent material, undergoes further softening during creep. Figure 5 and Table I illustrate the hardness (HV value on the softer surface of the gauge length of crept samples) variation with creep time (t_e) at 250 and 315°C.

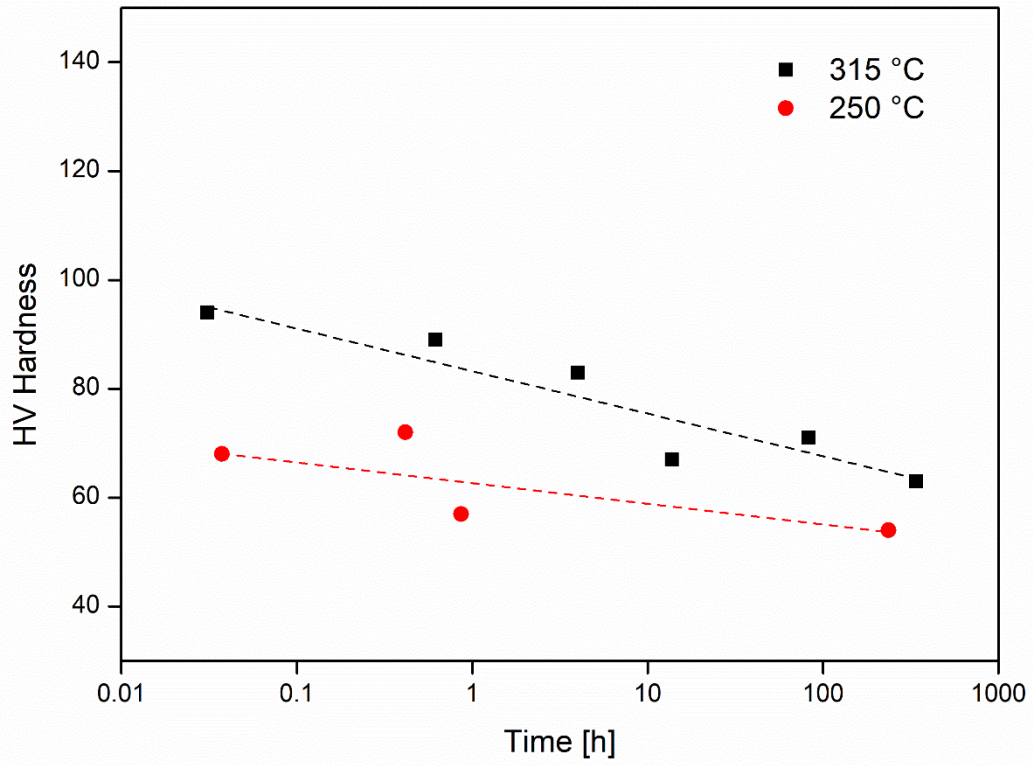

Figure 5. Hardness variation as a function of time of exposure (creep test duration) for the sample tested at 250 and 315°C.

Table I. Summary of the experimental results. The strain rate values reported in italic font were those of the VLE. Vickers hardness was measured at room temperature after testing.

T [°C]	Load sequence [MPa]	$\dot{\varepsilon}_m$ [s^{-1}]	t_e [h]	HV	λ [nm]	F_v [%]	N_v [μm^{-3}]
250	30	$4.0 \cdot 10^{-9}$	337	63± 1.0	550	0.06	1
	50-70-100	$1.8 \cdot 10^{-7}$-*$2.5 \cdot 10^{-6}$*-*$1.2 \cdot 10^{-4}$*	82.7	71 ± 0.6	-	-	-
	70	$7.2 \cdot 10^{-7}$	13.8	67 ± 2.4	-	-	-
	100	$2.5 \cdot 10^{-6}$	4.0	83 ± 1.0	190	0.74	26
	120	$8.6 \cdot 10^{-6}$	0.62	89 ± 0.5	-	-	-
	140	$2.6 \cdot 10^{-4}$	0.03	94 ± 0.5	110	1.73	138
	140	$7.3 \cdot 10^{-5}$	0.98	88± 0.5	-	-	-
315	12-50	$6.0 \cdot 10^{-9}$-*$4.5 \cdot 10^{-6}$*	237	54 ± 1.9	-	-	-
	25	$8.1 \cdot 10^{-7}$	0.87	57 ± 0.6	-	-	-
	40	$1.0 \cdot 10^{-5}$	0.42	72 ± 0.6	-	-	-
	60	$2.2 \cdot 10^{-4}$	0.04	68 ± 0.6	-	-	-

At the lowest temperature, a marked decrease in hardness is observed for times above 5 h. Although a linear description has been reported in the semi-logarithmic plot in Figure 5, the experimental trend of the HV *vs* t_e curve is better described by a curve of sigmoidal shape. In the case of the samples tested at the highest temperature, hardness remains invariably low, and just a moderate further decrease in HV can be observed. Figure 6 shows the hardness as a function of temperature compensated time (t_c), expressed as (Eq. (3)):

$$t_c = t_e \exp\left(-\frac{Q}{RT}\right) \qquad (3)$$

The hardness data, with Q=260 kJ mol^{-1}, collapse on a single master curve, that can be profitably used to recalculate the hardness value for the different experimental conditions.

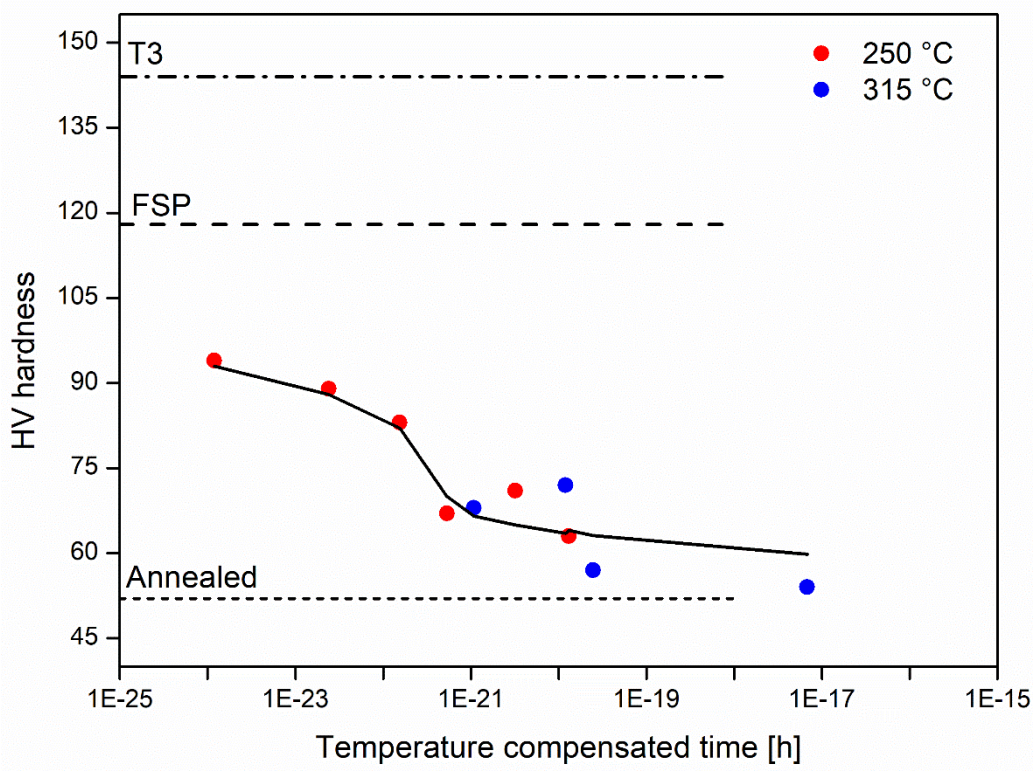

Figure 6. Hardness variation as a function of the temperature-compensated time, with Q =260 kJ mol^{-1}. The data substantially overlap on the same sigmoidal curve. The Figure also shows the hardness value for the T3 state, for the alloy after FSP, and for the fully annealed condition [18].

The reasons for the decrease in hardness clearly illustrated in Figures 5 and 6, can be easily found by analyzing the particle distribution after creep (Figures 7-9, Table I). The table shows the interparticle spacing of the intragranular strengthening precipitates (λ), the respective volume fraction (F_v) and their number per unit volume (N_v). Figures 7 and 8 clearly shows the typical rod morphology of the precipitates, typically aligned along the (200)-Al crystallographic direction. With this regard, the almost equiaxed precipitates visible in the TEM micrographs of Figures 7-to-9 are actually rods laying along the (002)-Al direction, *i.e.* along the electron beam direction.

The dramatic reduction of the volume fraction of intragranular precipitates, and their progressive loss of effectiveness as dislocation obstacles due to the very large interparticle distance (spacing, λ), are self-apparent. Other than these meaningful features, the precipitates mean dimensions were also affected by the different creep loads at 250°C. It is worth to mention here that the volume of the rod-

shaped precipitates did evolve primarily in their length. The lateral size ranged from 5 to 50 nm, while the thickness varied correspondingly only from 25 to 30 nm. On the other hand, the plate length greatly varied from typical minimum values of few tens to maximum of thousands of nanometers. Thence, Figure 10 reports the cumulative size distribution of the plate length for the creep loads of 30, 100, and 140 MPa at 250°C, corresponding to the conditions inspected by TEM, which are representatively reported in Figure 9. It is apparent that the mean particle length reduced to almost half from 30 to 140 MPa, with concurrent dramatic volume fraction, F_V, increment of almost 30-times (see Table 1). The corresponding distribution appears to be rather similar among the three conditions spanning from ~10 to ~2600 nm.

Creep exposure at 315°C, as suggested by Figure 6, leads to an even more pronounced softening of the microstructure, which closely corresponds to the dissolution of the finest precipitates, and the residual presence of coarse rods (Figure 11), whose strengthening effect is limited.

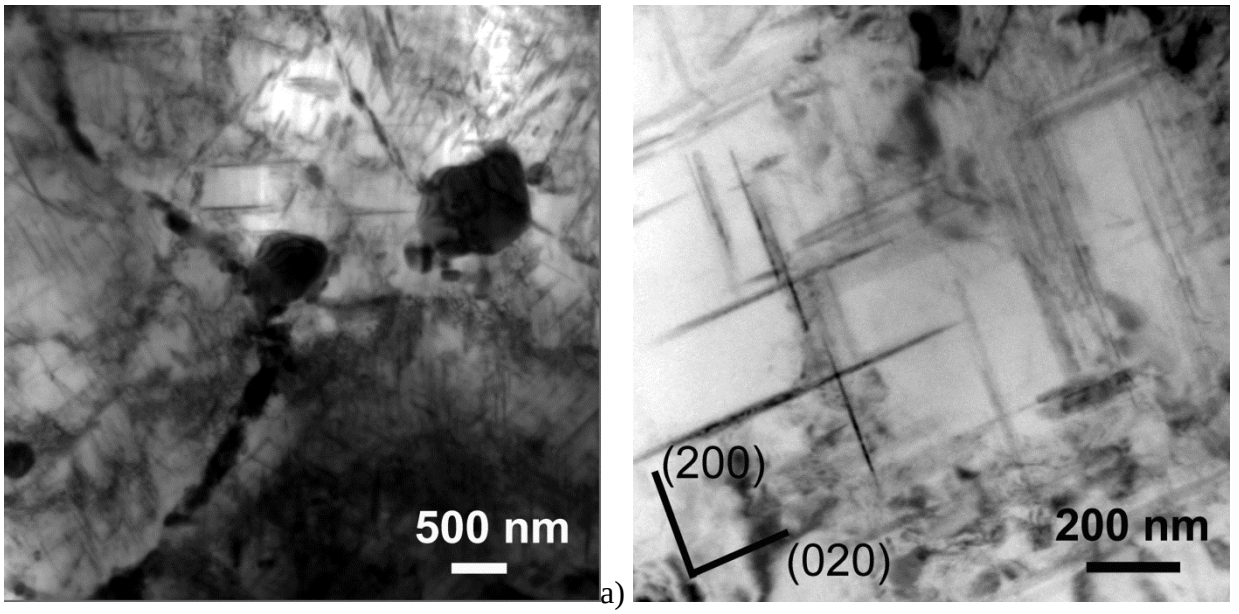

a) b)

Figure 7. Representative TEM micrographs of the sample tested under 140 MPa at 250°C. In a) the presence of large intergranular particles, either large precipitates or intermetallic phases, is well documented; in b), an example of the fine intragranular precipitates is shown.

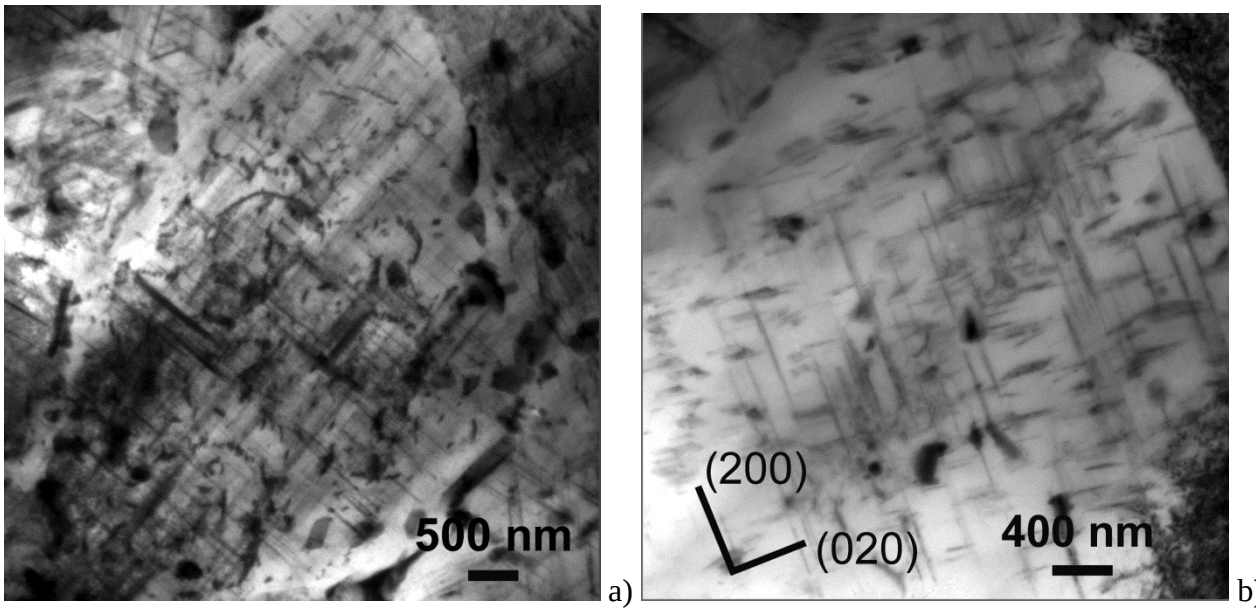

a) b)

Figure 8. Representative TEM micrographs of the sample tested under 100 MPa at 250°C. Comparison with Figure 7 indicates that the particle population is still densely distributed inside grains.

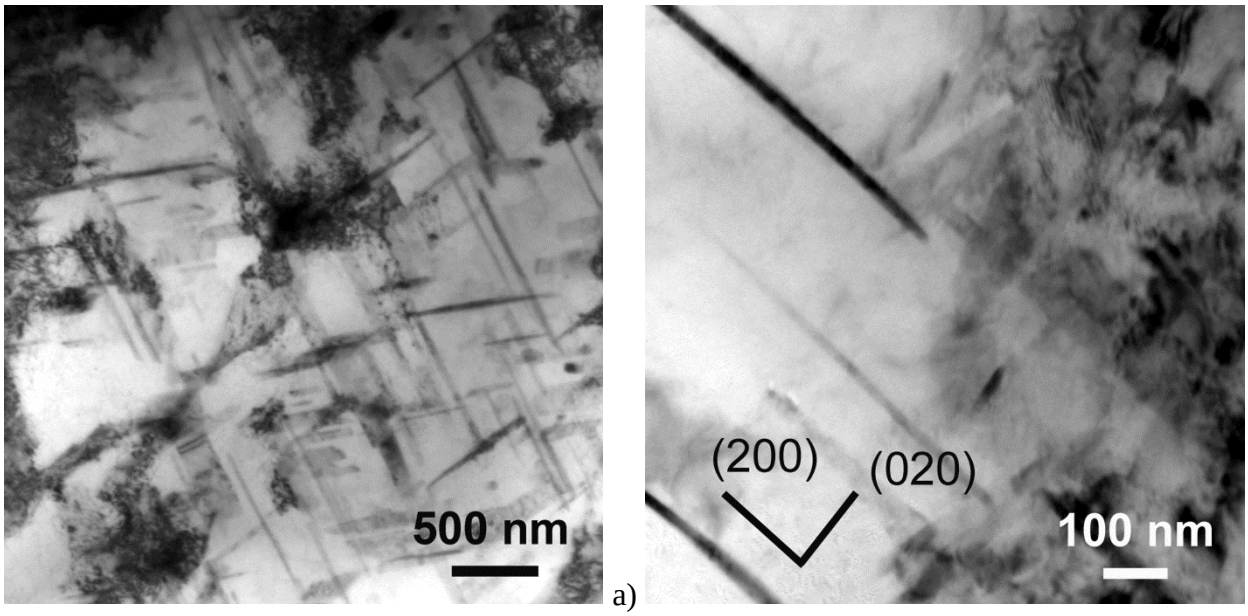

a) b)

Figure 9. Representative TEM micrographs of the sample tested under 30 and 50 MPa at 250°C. The long-time of exposure led to the progressive dissolution of the finest precipitates, and coarsening of the remaining ones.

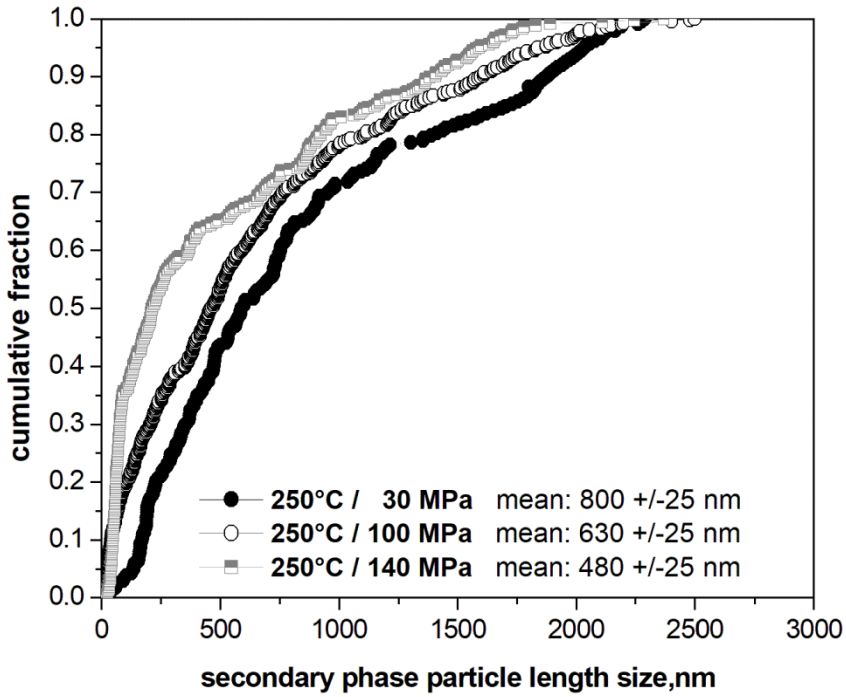

Figure 10. Distribution of the precipitates length, of the samples tested under 30, 100, and 140 MPa at 250°C, of which BF-TEM inspections of Figures 7- 9.

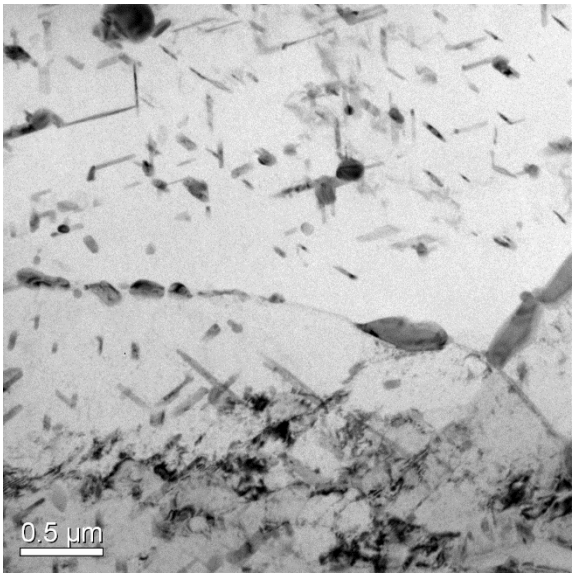

Figure 11. Representative TEM micrograph of the sample tested under 25 MPa at 315°C.

The Model

Equations for Dislocation Creep in Al: Strengthening Terms

The model, developed for Cu by Sandström [4-6], is based on the well-known Taylor equation, in the form (Eq. (4)):

$$\sigma_e = \sigma - \sigma_0 = \sigma_i + \sigma_{ss} + \sigma_\rho = \sigma_i + \sigma_{ss} + \alpha m G b \sqrt{\rho} \quad (4)$$

where m is the Taylor factor (m = 3.06 for fcc metals) and $\sigma_\rho = \alpha m G b \rho^{1/2}$ is the dislocation hardening term. The term σ_i represents the stress required to move a dislocation in the absence of other dislocations, and incorporates the effect of grain size, while α is a constant (in the following, α = 0.3 will be considered). The term σ_0 (conventionally denoted as "threshold stress") represents the strengthening contribution due to the interaction between particles, either precipitates, intermetallic phases or even oxides, and dislocations.

The stress σ_i, needed to move a dislocation in the annealed pure metal, was calculated by the equation (Eq. (5)) [10]:

$$\sigma_i = A_y \sqrt{\left(\sigma - \sigma_0 - \sigma_{ss} - \frac{k_{hp}}{\sqrt{d_g}} \right) G} + \frac{k_{hp}}{\sqrt{d_g}} \quad (5)$$

where d_g is the grain size, k_{hp} is the Hall-Petch constant, A_y = 0.0042 [7], σ is the stress under which the alloy creeps at the given strain rate, σ_0 and σ_{ss} are the precipitate and solid solution strengthening terms respectively.

The temperature and strain rate dependence of the Hall-Petch "constant" can be described by the phenomenological equation (Eq. (6)) [19]:

$$k_{hp}{}^2 = B_{hp} \exp\left(-\beta_{hp} T\right) \quad (6)$$

where B_{hp} is a constant (B_{hp}=86.5 MPa^2 mm^{-1}) and (Eq. (7)):

$$\beta_{hp} = \beta_0 - \beta_1 \ln \dot{\varepsilon} \quad (7)$$

with $\beta_0 \cong$0.003 K^{-1} and β_1=8x10^{-4} K^{-1} [10].

Solute atmospheres reduce dislocation mobility; the term σ_{ss} thus represents the stress required for dislocations to move through the viscous drag due to solute atoms (Cu and Mg in AA2024). Since

Cu and Mg mostly combine with Al to form the precipitates, the drag stress is here assumed to be very low, i.e. quite negligible in comparison with the other terms in Equation (4). On this basis, the assumption $\sigma_{ss} \cong 0$ will be used in the following.

Last, as above mentioned, the threshold stress σ_0 represents the strengthening contribution due to the interaction between fine precipitates and dislocations. In aged AA2024 alloy, the aluminium matrix is reinforced with a densely spaced distribution of precipitates. In Al-Cu-Mg alloys with Cu:Mg atomic ratio close to 1, the precipitation sequence is described as:

$$\alpha_{ss} \rightarrow \text{Cu:Mg co-clusters/GPB zones} \rightarrow \text{GPB2/S'' phase} \rightarrow \text{S'/S phase}$$

where α_{ss} is the super-saturated solid solution, GPB are the Guiner-Preston-Bagaryatsky zones and the S'' (GPB2) is an intermediate phase preceding the formation of the semicoherent S' phase [20]. The stable S-phase in the peak-aged state assumes the shape of non-shearable rods aligned in the {100} directions, although equiaxed precipitates can be also observed in the alloy after long creep exposure [21].

In general term, under high applied stress and/or at room temperature, the precipitate-strengthening effect is equivalent to the Orowan stress. Under low stresses, i.e. below the Orowan stress σ_{Or}, when Orowan by-pass cannot be operative, and high temperatures, dislocations can still overcome precipitates by different thermally activated mechanisms [10, 22-26]. A more detailed discussion on the subject has been reported in [9,10]. In the present instance, on the bases of the previous findings in [10], the precipitate strengthening term can be then expressed as (Eq. (8)):

$$\sigma_0 = \alpha_p \sigma_{Or} \qquad (8)$$

with, for the 2024-T3 alloy, α_p=0.7 and 0.55 at 250°C and 315°C respectively.

Rate Equation and Temperature Dependence

In the fine-grained alloy of the present study, the minimum creep rate dependence on applied stress and temperature is quite similar to that observed in the base material in T3 state, which had much

larger grains. The slope of the minimum creep rate vs applied stress curves is by too high to attest and important contribution of grain boundary sliding to deformation, an effect that can be explained by the pinning effect of the particles decorating grain boundaries. The analysis will be thus limited to dislocation-slip controlled deformation. Full details of the constitutive model derivation can be found in [10], and for this reason, only the final equations are given here.

The creep rate dependence on applied stress at steady state (assimilated to the minimum creep rate range) can be written as (Eq. (9)):

$$\dot{\varepsilon}_m = \frac{2M_{cg}\tau_l b\lambda}{m}\left(\frac{\sigma_\rho}{\alpha mGb}\right)^4 \qquad (9)$$

where λ is the interparticle spacing, τ_l is the dislocation line tension (τ_l=0.5Gb^2) and (Eq. (10)):

$$\sigma_\rho = \sigma - \sigma_0 - \sigma_i - \sigma_{ss} \cong \sigma - \sigma_0 = \sigma_e \qquad (10)$$

The dislocation mobility M can be expressed in the form (Eq. (11)):

$$M \cong \frac{D_{0L}b}{kT}\exp\left[\frac{\sigma_\rho b^3}{kT}\right]\exp\left\{-\frac{Q_L}{RT}\left[1-\left(\frac{\sigma_\rho}{R_{\max}}\right)^2\right]\right\}\exp\left(-\frac{U_{ss}}{RT}\right) \qquad (11)$$

where $R_{\max}$ is the maximum strength of the alloy, k is the Boltzmann constant, D_{0L} and Q_L are, respectively, the pre-exponential factor and the activation energy in the Arrhenius equation describing the temperature dependence of the vacancy diffusion coefficient. U_{ss} is a term describing the energy necessary for Cu and Mg atoms still in solid solution to jump in and out of the atmospheres that spontaneously form around dislocations (U_{ss} ≅14.5 kJ mol^{-1} [10]).

The maximum strength R_{max} at the testing temperature is here tentatively quantified as (Eq. (12)):

$$R_{\max} = \frac{1.5G\left(R^a_{UTS} + \sigma_{Or}\right)_{RT}}{G_{RT}} \qquad (12)$$

being R^a_{UTS} the tensile strength of an alloy with the same impurity level and similar content of elements in solid solution and coarse intergranular particles. The term σ_{Or} indicates the Orowan stress

generated by a dispersion of precipitates equivalent to that observed in the crept samples after testing; the RT suffix, in turns, denotes the room temperature values of the considered parameters (tensile strength, Orowan stress, shear modulus).

The strengthening role of the precipitates

The analysis of Eqns. (9) - (12) clearly suggests that the critical parameters to model the minimum creep rate dependence on applied stress are directly dependent upon the precipitates size and distribution. The σ_0 term, at high temperature, for example, can be considered to be proportional to the Orowan stress, which, in turns, depends on the interparticle spacing λ and to precipitate shape. The detailed analysis reported in [10] gave an excellent description of the experimental data for the 2024-T3 alloy, by assuming that all the precipitates were in forms of rods. In addition, the model also accounted for the stress accelerated coarsening process of the strengthening precipitates. It is obvious, that to properly use the model in this articulated and complex form, one should have a detailed knowledge of the microstructural evolution during creep exposure. In the case of the present study, a different approach was used, starting from the available information on the variation of hardness with creep time.

The Vickers hardness HV_{MPa} (expressed in MPa) of the alloy can be directly related to the yield stress (σ_y), by an equation in the form [27]:

$$\sigma_y = \beta_a \, HV_{MPa} - \beta_b \qquad (13)$$

where β_a and β_b are constants. Values for β_a for several Al-Mg-Si alloys, spanning from 0.266 to 0.383, with an average value of 0.303, are given in [27]. The β_b value can be thus calculated for the material investigated in the present study, by assuming β_a=0.303, and by considering that the same alloy in different states (T3 and FSP) has an HV_{MPa} hardness of 1411 and 1152 MPa respectively, for yield stresses of 362 and 284 MPa. This simple calculation gives β_b=65 MPa. Thus, one obtains, for

a 2024-O alloy (HV_{MPa} =510 MPa), a yield stress of 89 MPa, which is well in the range of the reported values (75-95 MPa [18]).

Equation (13) allows to obtain a reliable estimate of the yield stress of the alloy, starting from the HV values. Thus, the curve presented in Figure 6 can be used to calculate the yield stress of the crept microstructure.

The next step consists in estimating the contribution of the precipitates in the yield strength. At yielding, Eqn. (4) can be rewritten by explicitly introducing the Hall-Petch hardening term (σ_g), giving:

$$\sigma_y = \sigma_{i0} + \sigma_{ss} + \sigma_0 + \sigma_g + \alpha m G b \sqrt{\rho} \qquad (14)$$

where σ_{i0} is the stress necessary to move the dislocations in the pure metal with very coarse structure. In addition, one can reasonably assume that (Eq. (15)):

$$\sigma_y^a = \sigma_{i0} + \sigma_{ss} \qquad (15)$$

where σ_y^a is the yield strength of the matrix, that is, of a fully annealed large-grained alloy with comparable levels of impurities and elements in solid solution, and with massive precipitates on grain boundaries, thus giving, for the considered alloy (Eq. (16)):

$$\sigma_0 = \sigma_y - \sigma_y^a - \sigma_g - \alpha m G b \sqrt{\rho} \qquad (16)$$

Let one considers $\sigma_y^a \cong$55 MPa (yield stress for an alloy containing 0.5 Mg and 0.5 Mn) [18], σ_g being (Eq. (17)):

$$\sigma_g = \frac{k_{hp}}{\sqrt{d_g}} \qquad (17)$$

with k_{hp} =2.6 MPa mm$^{-0.5}$ [10] and d_g=5x10^{-3} mm; the last term to be determined for estimating the precipitate strengthening term from the curve presented in Figure 6, is the dislocation density. Creep is known to introduce dislocation densities which can be well above 10^{13} m^{-3} [7]; yet, after rupture, the samples considered in the present study remained in the furnace for a sufficiently long time to

consider that the free dislocation density underwent a substantial annealing. Thus, it is here assumed that ρ=1x10^{12} m^{-3}, irrespective of the applied stress or temperature. Then, Eqn. (16) provides the estimates of the precipitate strengthening term (in this case the Orowan stress, since room temperature data are considered) presented in Figure 10. These values can be considered to be reasonably accurate for the tests carried out in the low stress regime, where the dislocation density cannot be much larger than 1x10^{12} m^{-3}. The situation could be somewhat different for the tests carried out under the lower stresses at 250°C, where higher values of the dislocation density can be expected, leading to a reduced value of σ_0, that is, the values presented in Figure 11 could be overestimated. On the other hand, this effect is balanced by the fact that in the following it will be assumed that the microstructure at the end of the test was substantially equivalent to that corresponding to the minimum creep rate. For CLE tests carried out in the high stress regime, this would lead to an underestimation of the value of the precipitate strengthening term in correspondence to the minimum creep rate.

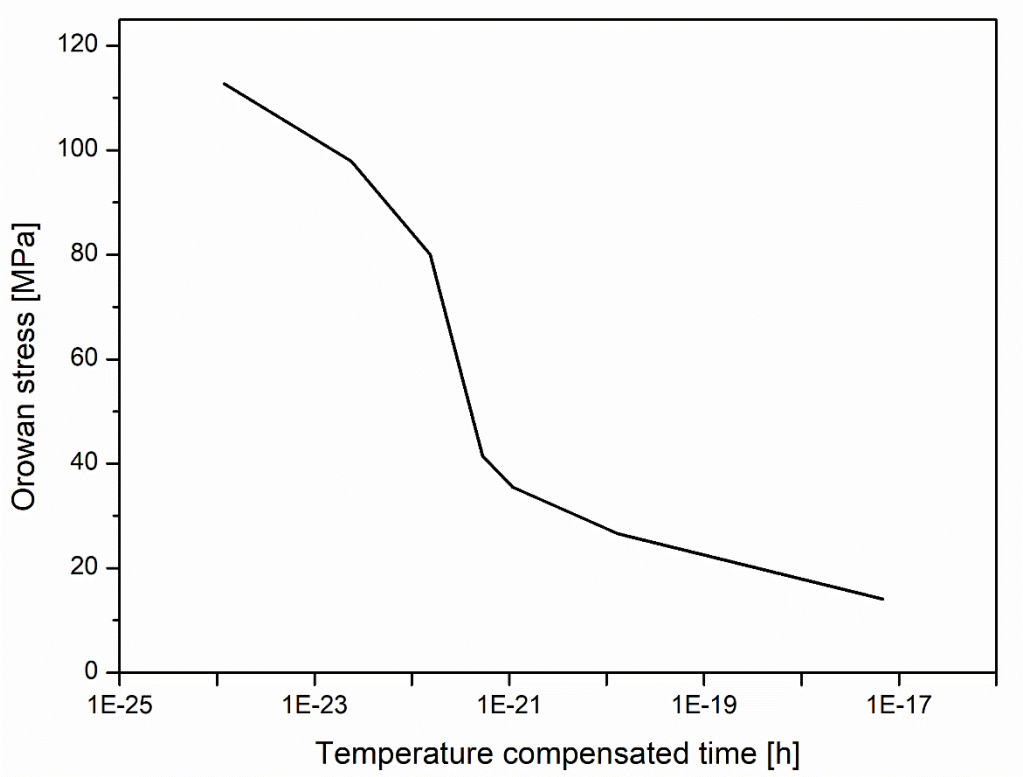

Figure 12. Precipitate (Orowan) strengthening term as a function of temperature compensated testing time.

The last missing major parameter in the model is the interparticle distance. The usual relationship between the Orowan stress and the interparticle spacing is of inverse proportionality. The interparticle values presented in Table I, the corresponding yield stresses from Fig. 12 and the best fitting straight line are presented in Figure 13, which can be then used to estimate λ for all the considered experimental conditions.

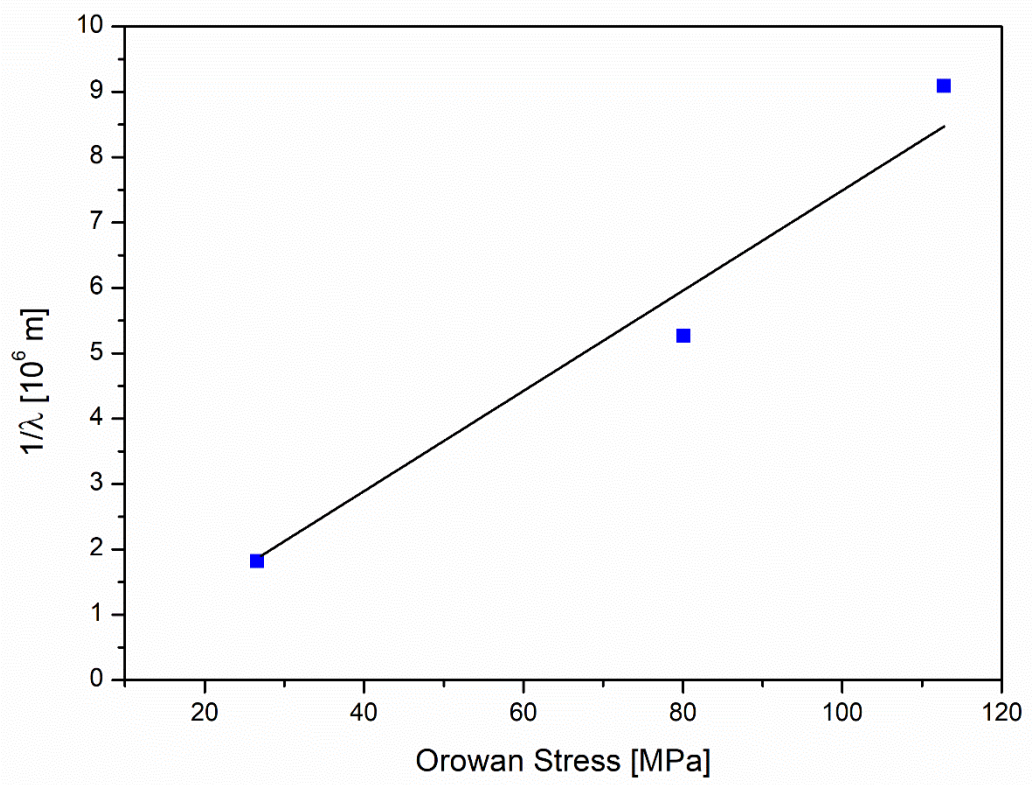

Figure 13. Reciprocal of precipitate-spacing as a function of the Orowan stress at room temperature.

At this stage, all the necessary information is available, and Eqns. (9) - (11) can be used, as in [10], with α_p = 0.7 and 0.55 at 250 and 315°C respectively, Q_{sd} = 122 kJ mol^{-1}, D_{0sd}= 8.3 × 10^{-6} m^2 s^{-1} and b=2.86x10^{-10}m. The calculated model curves for both CLE and VLE are reported in Figure 14. The curves for CLE data are actually obtained by connecting the value of the strain rate calculated for each stress, by assuming that the precipitate distribution in correspondence of the minimum creep rate is substantially equivalent to that observed after the end of the test. Thus, the curve connects strain rate values that correspond to different microstructures, namely different precipitate sizes and

distributions. By contrast, the curves modelling the VLE data, are obtained by assuming that the precipitate distribution for the whole loading sequence remains substantially unchanged, with respect to the one that could be observed in correspondence to the minimum creep rate under the first (and lowest) applied stress, just before load increase. Thus, each single VLE curve roughly corresponds to a constant microstructure, in terms of precipitate size and distribution. The description of the experimental data, which was obtained without any need of experimental minimum creep rate values data-fitting, is remarkably accurate, except under the highest stresses, i.e. in the region where a quite important scatter of the data was observed.

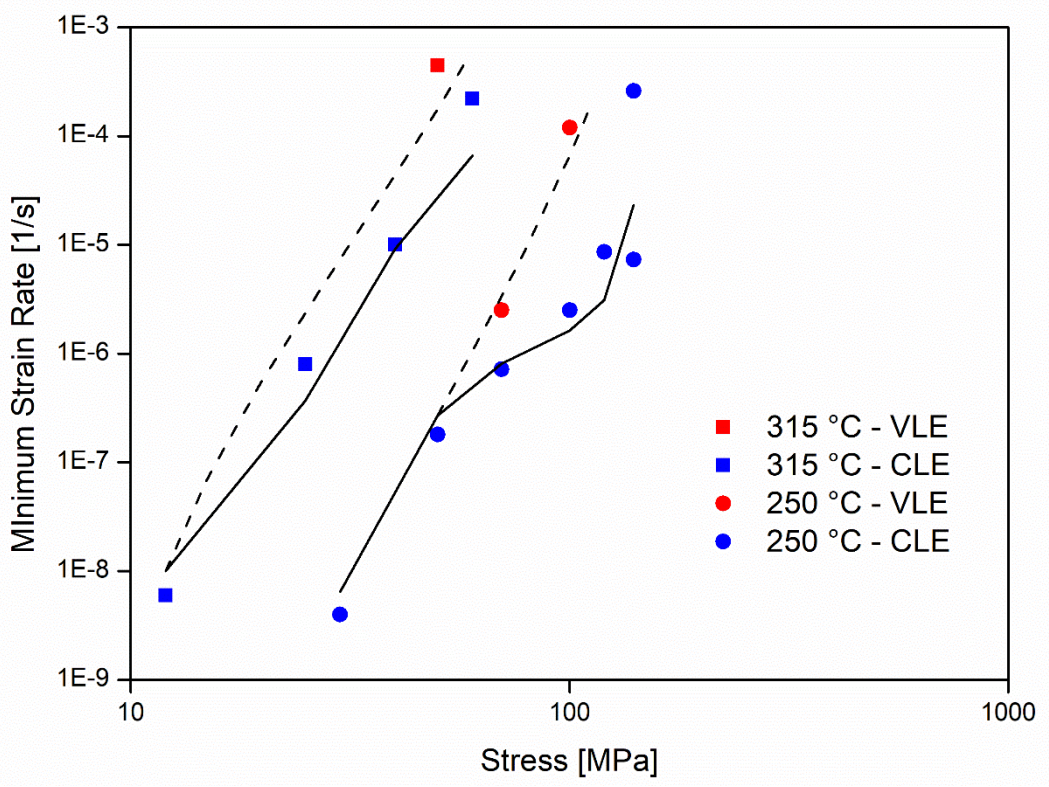

Figure 14. Basic creep modelling of the minimum strain rate dependence on applied stress for CLE (solid curves) and VLE (broken curves).

The analysis of Figure 13 definitely confirms that the model presented in [10] is an excellent tool for describing the creep response of age-hardening alloys. In addition, the accuracy of the description

suggests that the measure of the hardness variation after creep can give precious information to quantify the precipitate-strengthening term.

Conclusions

A constitutive model based on a theoretical approach has been used in the present study to describe the creep response of an AA2024-T3 alloy processed by FSP. The model, already successfully used for the description of the creep behaviour of the base alloy in –T3 state, was here applied to the transformed alloy with a fine recrystallized grain size and lower mechanical strength. The hardness variation with creep duration was used to quantify the precipitate strengthening term, in order to properly describe the softening phenomena associated to high-temperature exposure. The resulting model curves gave an excellent description of the experimental results, without requiring any data-fitting of the minimum creep rate experimental values, which represents a substantial advantage over conventional approaches based on phenomenological equations.

References

1. L. Kloc, E. Cerri, S. Spigarelli, E. Evangelista, T.G. Langdon, Significance of continuous precipitation during creep of a powder metallurgy aluminum alloy, Mater. Sci. Eng. A. 216 (1996) 161–168. https://doi.org/10.1016/0921-5093(96)10404-4.

2. L. Kloc, S. Spigarelli, E. Cerri, E. Evangelista, T.G. Langdon, Creep behavior of an aluminum 2024 alloy produced by powder metallurgy, Acta Mater. 45 (1997) 529–540. https://doi.org/10.1016/S1359-6454(96)00190-5.

3. S. Spigarelli, M. Cabibbo, E. Evangelista, T.G. Langdon, Creep properties of an Al-2024 composite reinforced with SiC particulates, Mater. Sci. Eng. A. 328 (2002) 39–47. https://doi.org/10.1016/S0921-5093(01)01698-7.

4. R. Sandström, Basic model for primary and secondary creep in copper, Acta Mater. 60 (2012) 314–322. https://doi.org/10.1016/j.actamat.2011.09.052.

5. R. Sandström, Influence of phosphorus on the tensile stress strain curves in copper, J. Nucl. Mater. 470 (2016) 290–296. https://doi.org/10.1016/j.jnucmat.2015.12.024.

6. R. Sandström, The role of cell structure during creep of cold worked copper, Mater. Sci. Eng. A. 674 (2016) 318–327. https://doi.org/10.1016/j.msea.2016.08.004.

7. S. Spigarelli, R. Sandstrom, Basic creep modelling of aluminum, Mater. Sci. Eng. A 711 (2018) 343-349. https://doi.org/10.1016/j.msea.2017.11.053.

8. S. Spigarelli, C. Paoletti, A unified physical model for creep and hot working of Al-Mg solid solution alloys, Metals 8 (2018) 9. https://doi.org/10.3390/met8010009.

9. S. Spigarelli, C. Paoletti, A new model for the description of creep behaviour of aluminium-based composites reinforced with nanosized particles, Compos. Part A Appl. Sci. Manuf. 112 (2018) 346-355. https://doi.org/10.1016/j.compositesa.2018.06.021.

10. C. Paoletti, M. Regev, S. Spigarelli, Modelling of creep in alloys strengthened by rod-shaped particles: Al-Cu-Mg age-hardenable alloys, Metals 8 (2018) 930. https://doi.org/10.3390/met8110930.

11. Y.C. Lin, Y.C. Xia, Y.Q. Jiang, L.T. Li, Precipitation in Al-Cu-Mg alloy during creep exposure, Mater. Sci. Eng. A. 556 (2012) 796–800. https://doi.org/10.1016/j.msea.2012.07.069.

12. Y.C. Lin, Y.C. Xia, Y.Q. Jiang, H.M. Zhou, L.T. Li, Precipitation hardening of 2024-T3 aluminum alloy during creep aging, Mater. Sci. Eng. A. 565 (2013) 420–429. https://doi.org/10.1016/j.msea.2012.12.058.

13. M. Regev, S. Spigarelli, Study of mechanical, microstructural and thermal stability properties of friction stir processed aluminum 2024-T3 alloy, Kovove Mater. 57 (2019) 229–236. https://doi.org/10.4149/km_2019_4_229.

14. R.S. Mishra, M.W. Mahoney, S.X. McFadden, N.A. Mara, A.K. Mukherjee, High strain rate superplasticity in a friction stir processed 7075 Al alloy, Scripta Mater. 42 (2000) 163-168. https://doi.org/10.1016/S1359-6462(99)00329-2.

15. N. Nadammal, S.V. Kailas, S. Suwash, A bottom-up approach for optimization of friction stir processing parameters; a study on aluminium 2024-T3 alloy, Mater. Des. 65 (2015) 127-138. https://doi.org/10.1016/j.matdes.2014.09.005.

16. R.L. Higginson, C.M. Sellars, Worked Examples in Quantitative Metallography, Maney Publishing, London, SW1Y 5DB, 2003, pp.82-91. ISBN: 1-902653-80-7.

17. M. Cabibbo, Microstructure strengthening mechanisms in different equal channel angular pressed aluminum alloys, Mater. Sci. Eng. A 560 (2013) 413-432. https://doi.org/10.1016/j.msea.2012.09.086.

18. J.R. Davis, Aluminum and Aluminum Alloys, first ed., ASM Specialty Handbook, ASM International, Materials park, Ohio, USA, 1993.

19. V.E. Panin, R.W. Armstring, Hall-Petch analysis for temperature and strain rate dependent deformation of polycrystalline lead, Phys. Mesomech. 19 (2016) 35-40.
https://doi.org/10.1134/S1029959916010045.

20. I.N. Khan, M.J. Starink, J.L. Yan, A model for precipitation kinetics and strengthening in Al-Cu-Mg alloys, Mater. Sci. Eng. A. 472 (2008) 66–74. https://doi.org/10.1016/j.msea.2007.03.033.

21. M. Regev, T. Rashkovsky, M. Cabibbo, S. Spigarelli, Microstructure Stability During Creep of Friction Stir Welded AA2024-T3 Alloy, J. Mater. Eng. Perform. 27 (2018) 5054-5063. https://doi.org/10.1007/s11665-017-3122-8.

22. M.E. Kassner, M.-T. Pérez-Prado, Five-power-law creep in single phase metals and alloys, Prog. Mater. Sci. 45 (2000) 1–102. https://doi.org/10.1016/S0079-6425(99)00006-7.

23. W. Blum, B. Reppich, Creep of particle-strengthened alloys, in: B. Wilshire, R.W. Evans, Creep behavior of Crystalline Solids, first ed., Pineridge Press, Swansea, UK, 1985 pp. 83-135.

24. M. Heilmaier, B. Reppich, Particle threshold stresses in high temperature yielding and creep: a critical review, in: R.S. Mishra, A.K. Mukherjee, K.L. Murty, Creep behavior of the advanced materials for 21st century, TMS, 1999, pp. 267-281.

25. J. Rösler, E. Arzt, A new model-based equation for dispersion strengthened materials, Acta Metall. Mater. 38 (1990) 671-683. https://doi.org/10.1016/0956-7151(90)90223-4.

26. J. Rösler, R. Joos, E. Arzt, Microstructure and creep properties of dispersion-strengthened aluminum alloys, Metall. Trans. A 33 (1992) 1521-1539. https://doi.org/10.1007/BF02647335.

27. A.P. Sekhar, S. Nandy, K. Kumar Ray, D. Das, Hardness-Yield strength relation of Al-Mg-Si alloys, IOP Conf. Series: Materials Science and Engineering 338 (2018) 012011.